The Mechanical Stability of a Salt Cavern

Used for Compressed Air Energy Storage (CAES)

Hippolyte Djizanne & Pierre Bérest, LMS, Ecole Polytechnique Paris Tech, Palaiseau, France

Benoît Brouard, Brouard Consulting, Paris, France

THE MECHANICAL STABILITY OF A SALT CAVERN
USED FOR COMPRESSED AIR ENERGY STORAGE (CAES)

Hippolyte Djizanne[1], Pierre Bérest[1], Benoit Brouard[2]

(1) LMS, Ecole Polytechnique ParisTech, Palaiseau, France

(2) Brouard Consulting, Paris, France

Abstract

Compressed Air Energy Storage (CAES) in salt caverns has been successful at two sites for 35 years. This technology remains relevant with the increasing interest in renewable energy, as it represents an interesting option for massive energy storage. The most significant improvement in recent years is most likely the third generation of CAES, or AA-CAES, in which the storage of compressed air is adiabatic, allowing the energy balance to be optimized during operation and increased overall efficiency of the facility. From the perspective of rock mechanics, there are still questions about the structural stability of a cavern under high-frequency loading. Several researchers work in both the experimental and numerical aspects: for experimental aspects, see Arnold et al. (2011), Bauer et al. (2010, 2011), and Fuenkajorn and Phueakphum (2009); for numerical aspects see Staudtmeister and Zapf (2010), Dresen and Lux (2011), Brouard et al. (2007, 2011) and Bérest et al. (2012). This paper presents numerical computations performed to analyze the stability of overhanging blocks, especially during debrining and at an early stage.

Key words: CAES, Overhanging Blocks, Debrining, Air Lift, Numerical Computations, Rock Mechanics

1. Introduction

Salt caverns used for underground storage of large quantities of gas are stretched to face ever-increasing energy needs. Indeed, these caverns now are used on an almost daily basis. Thus, the interest in storage has increased, as has the variability of stored products. In addition to natural gas, hydrogen and compressed air used to generate electricity also are stored.

These new salt-cavern operating modes raise new mechanical issues, particularly illustrated by spalling observed at the walls of some existing caverns. In fact, purely mechanical stresses related to changes in gas pressure, overlapping variations in temperature of several tens of °C, which cause additional tensile stresses, may generate fractures at the cavern wall. This process must be understood. During debrining, for example, brine is replaced by gas that is less dense, which allows study of whether a buoyancy effect may explain blocks falls.

The purpose of this paper is to explain why and when overhanging blocks fall. A realistic CAES cavern is considered. A highly refined mesh is used at the vicinity of the cavern wall to take into account the effects of thermoelastic stresses during rapid loading or unloading. The mechanical stability of the cavern is discussed at four key moments: (1) during debrining, (2) during rapid withdrawal, (3) during rapid injection, and (4) during an air lift. The mechanical behavior of salt is considered as elasto-viscoplastic and is highly sensitive to temperature variation; hence the Munson Dawson (M-D) model is selected. The onset of dilation and tensile effective stresses in the blocks are discussed.

2. Lessons drawn from a real cavern (Huntorf, Germany)

In a remarkable paper, Crotogino et al. (2001), described "*more than 20 years of successful operation*" of the CAES storage at Huntorf (Germany). Two caverns having depths between 650 m and 800 m were operated. The air pressure varied between 4.3 and 7 MPa (600 and 1000 psi). The fastest depressurization rate was 5 MPa/hr (700 psi/hr). Between 1978 and 1986, there were 200 starts every year between 1978 and 1986, and less than 100 starts per year in the 1990s.

Quast (1983) compared two vertical cross-sections of the NK1 cavern (see Figure 1), which had been run in 1976 (filled with brine) and four years later in 1980 (filled with gas). His opinion was that the (laser) 1980 sonar survey correctly reflects the actual shape of the cavern. Salt "curtains", still present in 1976 when the cavern was filled with brine, broke and fell to cavern bottom during the first gas injection (during which the cavern bottom raised by 16 m). Later, the depth of the brine-air interface remained almost constant, and Crotogino et al. (2001), stated that "*evaluations over the whole operational period shows practically no changes that can be attributed to roof falls*" (p. 356). Although laser sonar could not be performed routinely,

> "*when cavern NK1 was expanded to atmospheric pressure at the beginning of 2001, a survey was possible with a heated laser tool … The evaluation of this survey after over 20 years of operation showed practically no deviation compared to the original conditions*" (p.356).
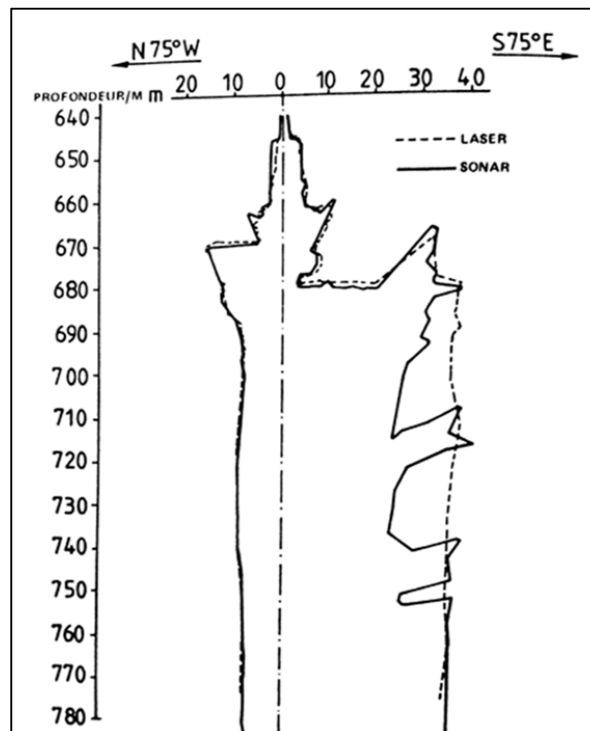

Figure 1. Huntorf Cavern: Comparison between 1976 sonar survey (cavern filled with brine) and 1980 sonar survey (cavern filled with gas) (Quast, 1983).

3. Numerical computations

Numerical computations were performed using the LOCAS software program (Brouard et al., 2006), which allows fully-coupled thermo-hydro-mechanical computations of gas or liquid-filled caverns.

3.1 Geometrical model

A 282,400-m^3 axisymmetric, compressed air-filled cavern is considered (Figure 2). The top of the cavern is at a 650-m depth, and the cavern is 150-m high. The cavern shape is taken from Huntorf NK1 cavern shape in 1976. (Note: we do not intend to model the Huntorf NK1 cavern; this shape was chosen because it is typical of a cavern with overhanging blocks.)

Table 1 provides the geometrical characteristics of the cavity under study.
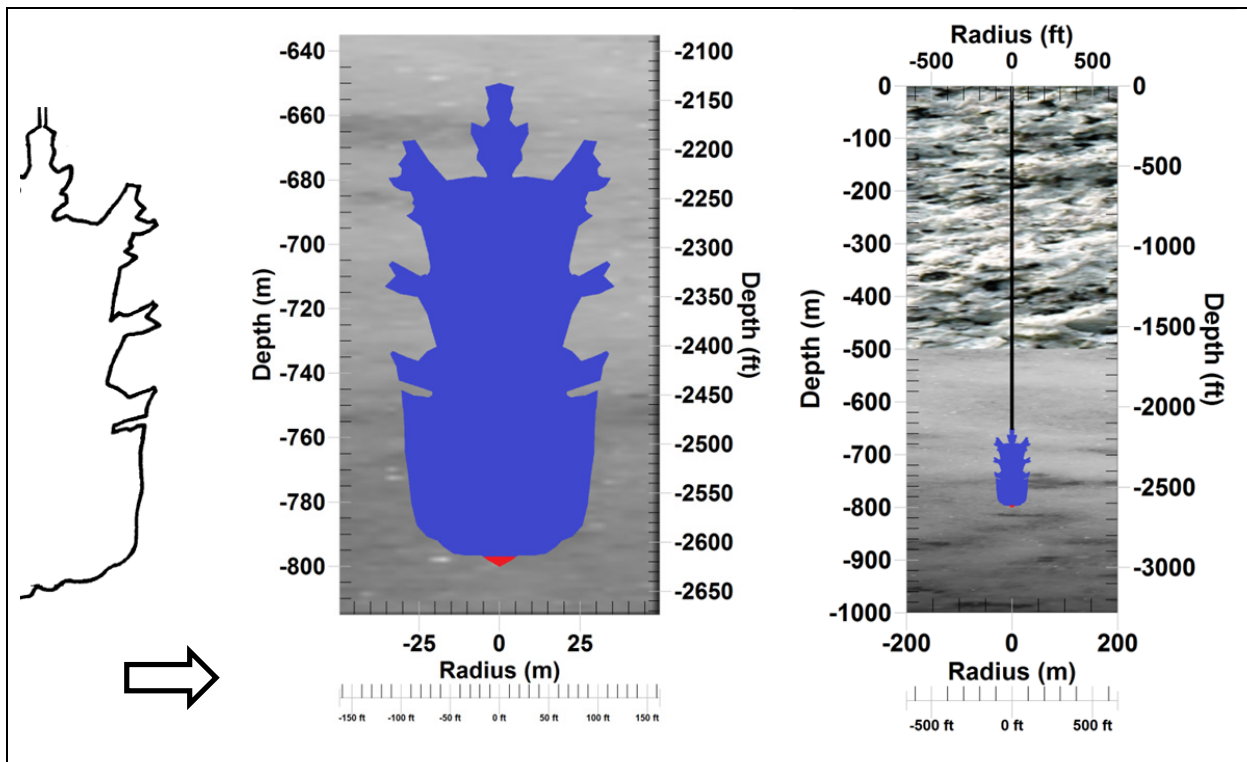

Figure 2. 2D axisymmetric cavern shape inspired from the Huntorf NK1 sonar (After Crotogino et al., 2001).

Table 1. Cavern geometrical properties.

Free Volume (m^3)	Air Volume (%)	Brine Volume (%)	Cavern Height (m)	Average Diameter (m)	Cavern Top (m)	Sump depth (m)	Average depth (m)	Cavern bottom (m)
281,486	99.96	0.04	150	79.88	650	797	725	800

3.2 Compressed air cavern

Compressed air is used in this paper as the stored gas. The thermodynamic properties of air are provided in Table 2.

Table 2. Thermodynamic properties of air.

Properties	Unit	Value
Reference temperature	K	295.15
Reference pressure	MPa	0.1
Density	kg/m^3	1.2
Heat capacity at constant pressure	J-kg-K	1001.7
Heat capacity at constant volume	J-kg-K	690.8
Ratio C_p/C_v	–	1.45
Dynamic viscosity	x 10^{-5} Pa.s	1.695

3.3 Stratigraphy

Table 3 shows the considered stratigraphy.

Table 3. Considered site stratigraphy.

N°	Rock	Thickness (m)	Density (kg/m^3)	Young's modulus (GPa)	Poisson's ratio (-)	Thermal conductivity (W/m-K)
1	Clay	500	2520	8.6	0.23	3
2	Salt	500	2200	$E_{salt} = 30$	$v_{salt} = 0.25$	6.1

3.4 Boundary conditions

The geostatic pressure and the geothermal temperature as functions of depth are given in Figure 3. The geostatic pressure and the geothermal temperature at cavern mid-depth are 15.65 MPa and 31.1°C, respectively. The geostatic pressure is fixed 200 m from the cavern axis.
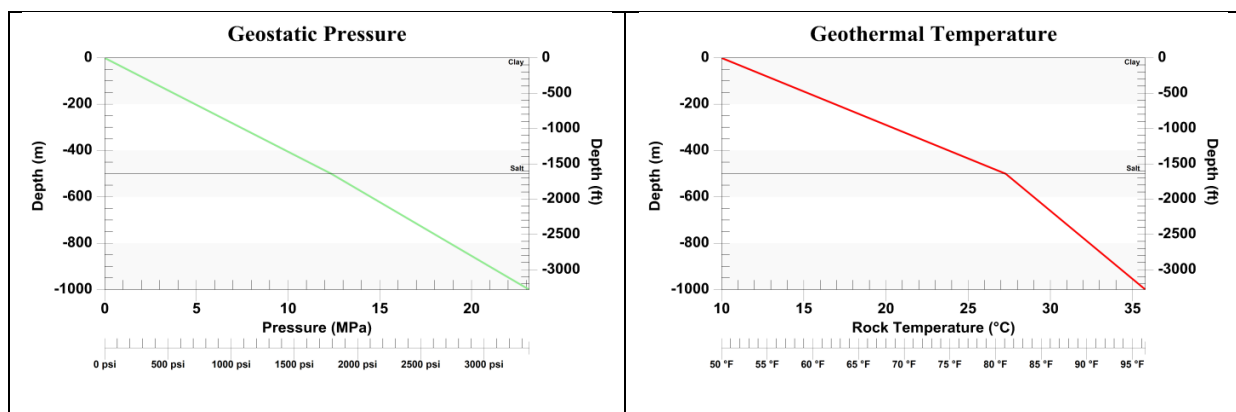

Figure 3. Geostatic pressure (left) and geothermal temperature (right) vs depth.

4

3.5 Meshing

The meshed area is 1000-m (3000-ft) high and 200-m (656-ft) wide. The meshing is subdivided into three parts. Close to the cavern wall (a few meters), there is an increased high-density area in which the maximum distance between nodes on the cavern wall is 0.25 m (10 in). Then, there is a normal high-density area, in which the maximum size of elements is 3 m (10 ft). Finally, there is a low-density area in which the maximum size of the elements is 10 m. The mesh used for numerical computations is shown in Figure 4: the number of mesh elements is 82,022, and the number of nodes is 41,775. One point in Block #1 (the red dot in Figure 4) is selected for further analysis.

3.6 Constitutive law

The Munson-Dawson (M-D) constitutive law (1984) is used to describe the behavior of salt. Two differential equations comprise the M-D model: (1) the strain-rate equation, which gives the viscoplastic strain rates; and (2) the evolutionary equation, which gives the rate of change of an internal variable. The three-dimensional form of the M-D model is given below:

$$\dot{\varepsilon}^{ij} = \dot{\varepsilon}_e^{ij} + F\dot{\varepsilon}_{ss}^{ij} \quad \begin{aligned} F &= e^{\Delta\left(1-\varsigma/\varepsilon_t^*\right)^2} & \text{when } \varsigma \leq \varepsilon_t^* \\ F &= e^{-\delta\left(1-\varsigma/\varepsilon_t^*\right)^2} & \text{when } \varsigma \geq \varepsilon_t^* \end{aligned} \tag{1}$$

$$\begin{cases} \dot{\varsigma} = (F-1)\dot{\varepsilon}_{ss} \quad \dot{\varepsilon}_{ss} = A\exp\left(-\dfrac{Q}{RT_{salt}}\right)\left(\sqrt{3J_2}\right)^n \quad \mu = E_{salt}/2(1+\nu_{salt}) \\ \varepsilon_t^* = K_0 e^{cT}\sigma^m \quad \Delta = \alpha_w + \beta_w Log_{10}(\sigma/\mu) \quad \sigma = \sqrt{3J_2} \end{cases} \tag{2}$$

Considered parameters for this constitutive law are given in Table 4. $\left(E_{salt}, \nu_{salt}\right)$ are salt elastic parameters.

Table 4. Considered Munson-Dawson creep parameters.

A (/MPa^n-yr)	n	Q/R (K)	m	α_w	β_w	K_0 (/MPa^m-yr)	δ	c (/K)
0.64	3.1	4100	3	-13.2	-7.738	7×10^{-7}	0.58	0.00902

3.7 Stability — failure criteria

When working with fast pressure changes, cycling loading and cavern stability, the onset of tensile stresses and salt dilation at the cavern wall must be discussed.

3.7.1 No Effective-Stress criterion

The No Effective-Stress criterion (Brouard et al., 2007; Djizanne et al., 2012) stipulates that the effective tangential stresses, σ_{eff}, at the cavern wall must be negative — i.e., compressive:

$$\sigma_{eff} = \sigma_{tt} + P < 0 \tag{3}$$

where σ_{tt} is the least compressive tangential stress. This criterion is much more demanding than a no-tension criterion. In some circumstances, when a gas-filled cavern is submitted to a fast and large pressure increase, this criterion is not met. It is noted that the relevance of this criterion has not been investigated fully.
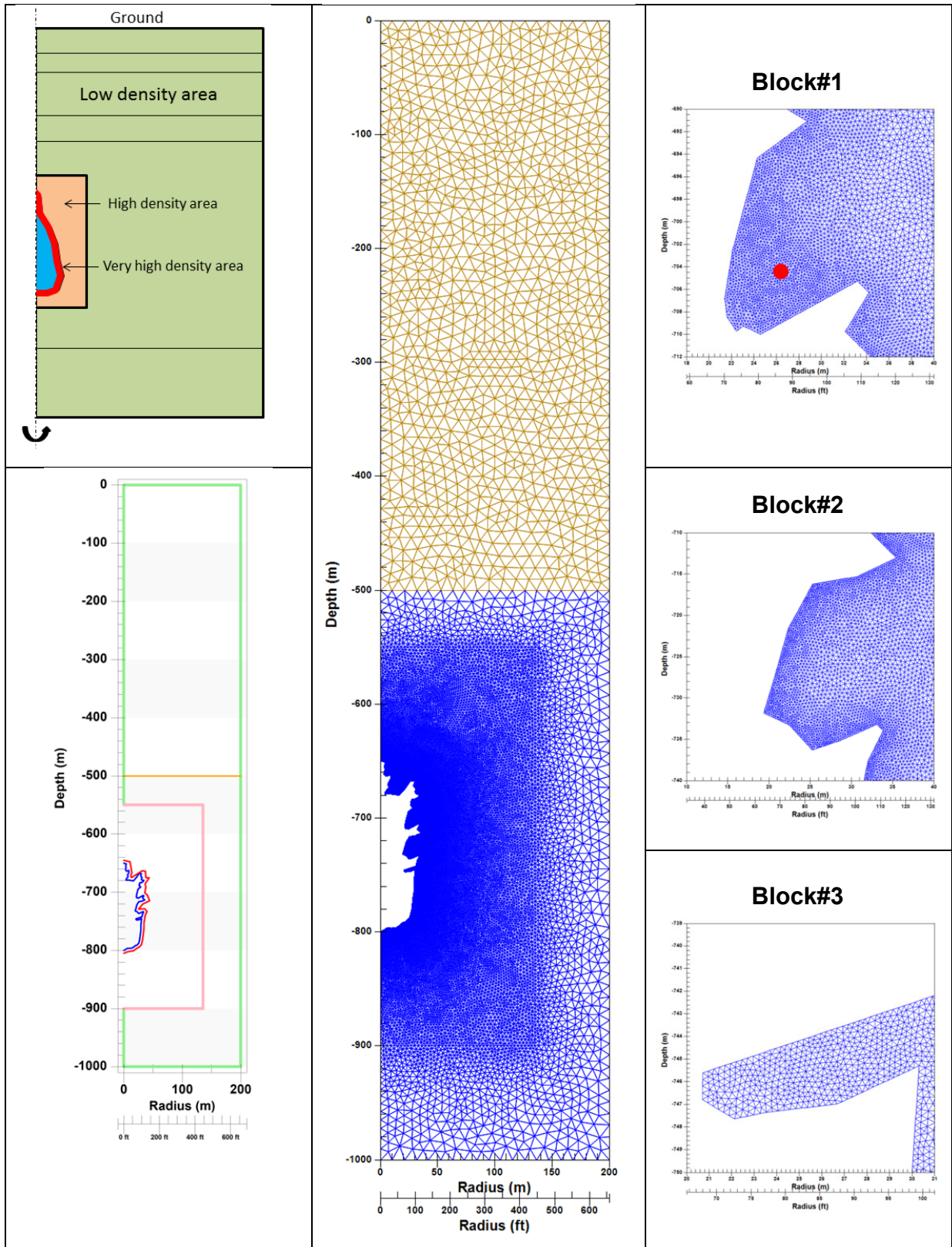
Figure 4. Model meshing.

3.7.2 Dilation criterion

When shear stresses are large compared to the mean stress, salt micro-fracturing and dilation can occur. Dilation leads to an increase in permeability and a loss of rock strength. Various criteria for the onset of salt dilation can be found in the literature (Spiers, 1988; Van Sambeek, 1993; DeVries et al., 2003; and Critescu and Hunsche, 1998, among many others). A rapid comparison of several criteria in the plane of invariants, or stress space, is shown in **Erreur ! Source du renvoi introuvable.**.
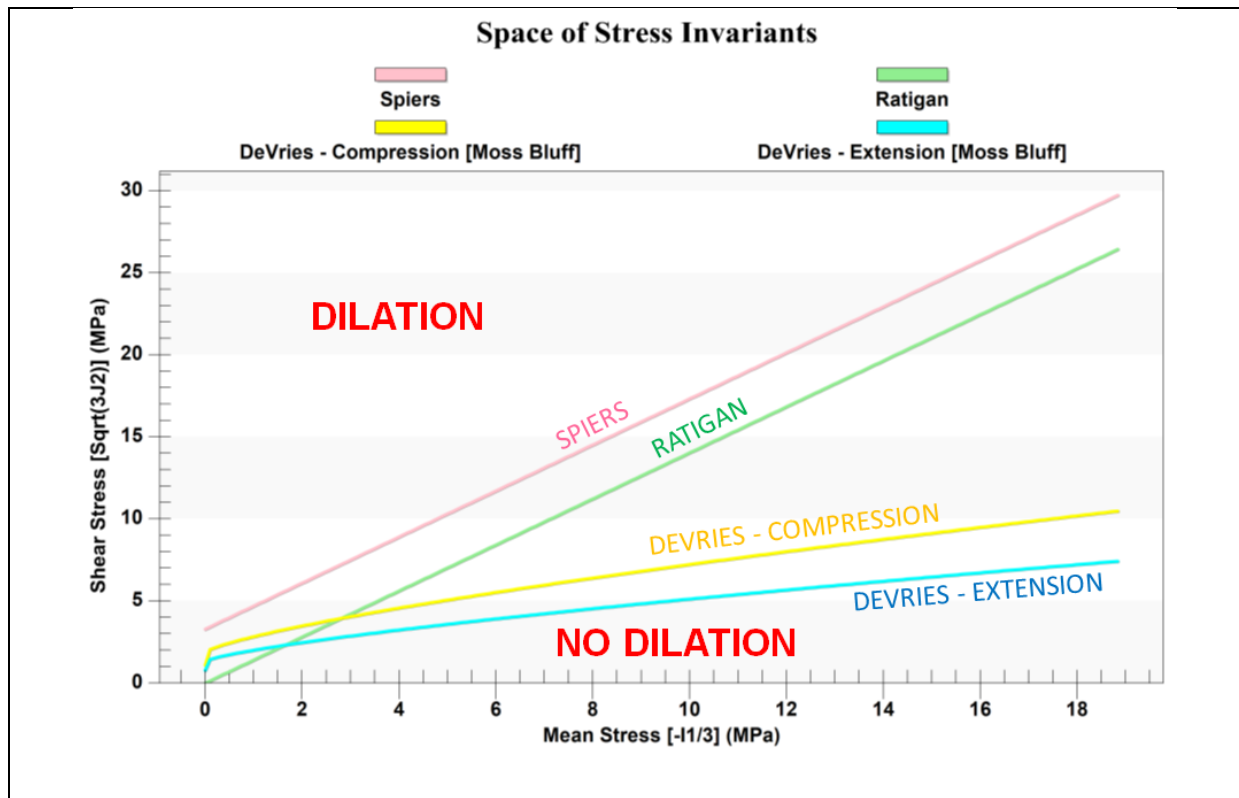
Figure 5. Comparison of several dilation criteria in the stress space.

The DeVries dilation criterion (RD, DeVries et al., 2003) was selected. Its formulation is as follows:

$$\sqrt{J_2} < \sqrt{J_2}_{dil} = \frac{D_1\left(\frac{I_1}{\text{sgn}(I_1)\sigma_0}\right)^{n_1} + T_0}{\left(\sqrt{3}\cos\psi - D_2\sin\psi\right)} \qquad \text{FOS} = \frac{\sqrt{J_2}_{dil}}{\sqrt{J_2}} \qquad (4)$$

where I_1 is the mean stress, J_2 is the second invariant of the stress tensor, ψ is the lode angle, $\sigma_0 = 1$ MPa, and $\left(D_1, D_2, n_1, T_0\right)$ are salt-specific parameters. This formula defines a factor of safety, FOS. There is no dilatancy when $FOS > 1$. The considered values of the parameters for this criterion are given in Table 5.

Table 5. Considered parameters of the DeVries dilation criterion.

n_1	D_1 (MPa)	D_2	T_0 (MPa)	σ_0 (MPa)
0.75	0.683	0.512	1.351	1

3.8 Cavern loading

The considered evolution of cavern pressure is shown on Figure 6. Cavern leaching lasts 1000 days, followed by a 900-day stand-by period at constant pressure. Cavern debrining from beginning to end (points A-B in the Figure 6) lasts 100 days. At the end of debrining, the cavern is discharged to the atmospheric pressure (point C). As seen through points C to D, air is injected to reach 8 MPa (1160 psi) after 10 days. The air-entry temperature during this injection is assumed to be 36°C (97 °F).
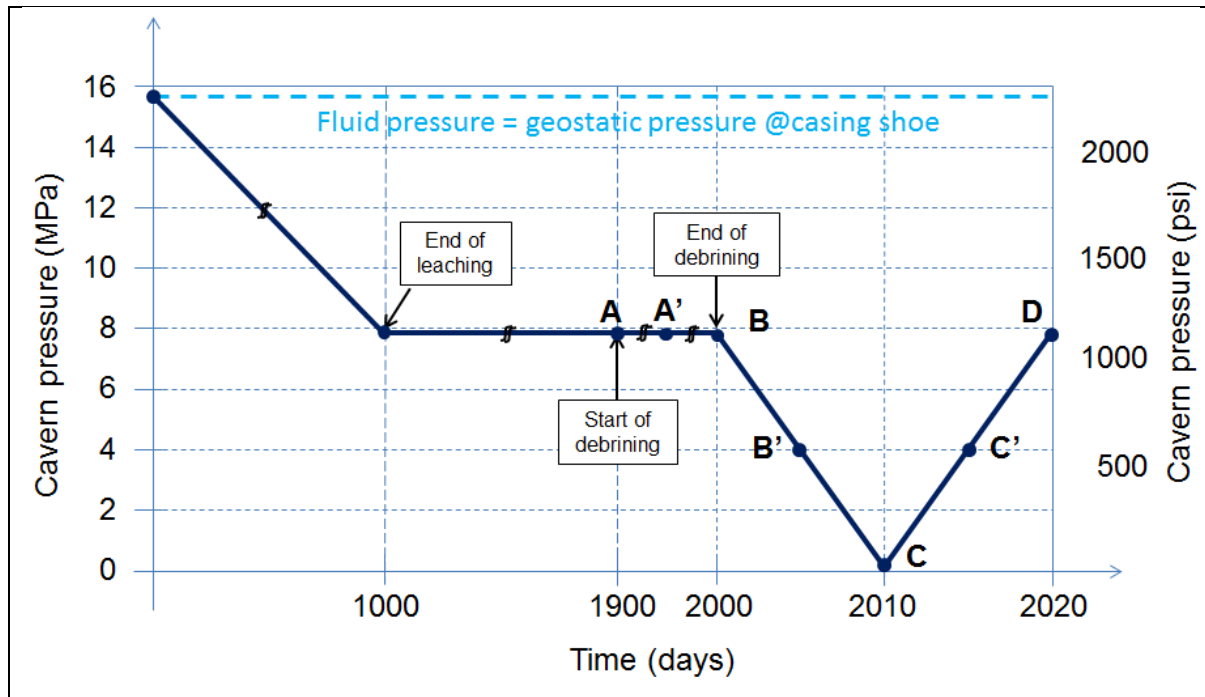

Figure 6. Considered evolution of pressure at the cavern top: from B to C, the depressurization rate is -0.8 MPa/day (-116 psi/day); from C to D, the repressurization rate is symmetrical (+0.8 MPa/day, or 116 psi/day).

4. Computations results

4.1 Mechanical stability during debrining AB

The cavern pressure is kept constant during the debrining operations: air is injected in the annulus while brine is expelled from the tubing at ground level. According to Archimedes' principle, as brine is replaced by air during debrining, the buoyant force is reduced and may create horizontal tensile stresses? at the upper part of overhanging blocks (see the Appendix).

Figure 7 shows effective-stress contours during the debrining. There are no large areas where effective stress is tensile.

Figure 8 shows a close-up of the effective-stress contours when looking at overhanging block #2 when in brine (left) and when in air (right). There is no tensile effective stress at the cavern wall even when the effective stress is close to zero along the wall. However, this configuration might be unstable, as the tensile zone may enlarge when a fracture develops.

Displacements of the same block during debrining are given in Figure 9 (left). The right side of Figure 9 shows orientations of principal stresses that are all compressive in the block at the end of debrining.
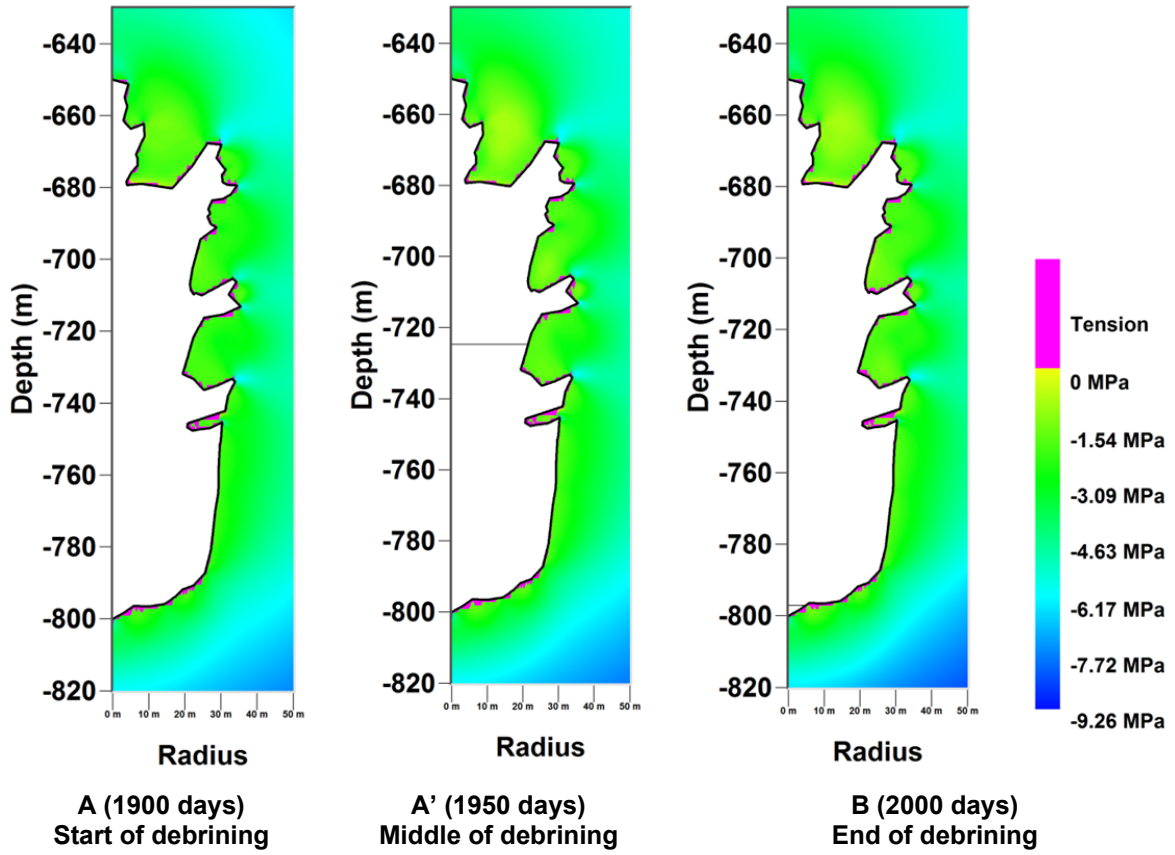
8

Figure 7 . Effective-stress contours during debrining AB.
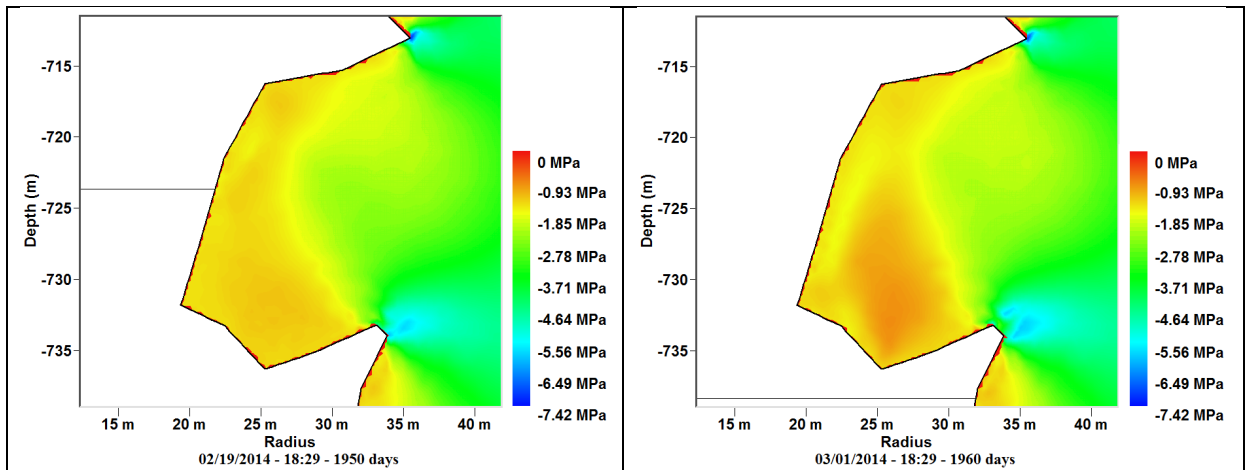

Figure 8. Close-up (Block #2): Effective-stress contours during debrining, when the air/brine interface (horizontal line) is at 724-m depth at 1950 days (left) and when at 738-m depth at 1960 days (right).
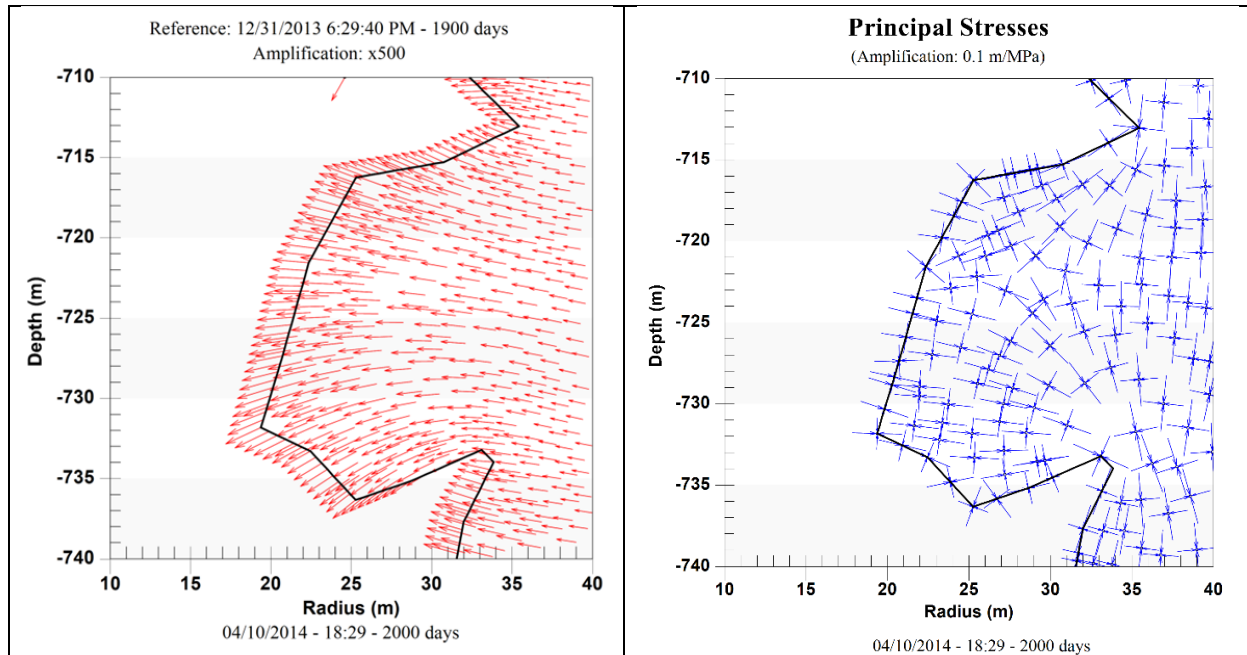
Figure 9. Close-up (Block #2): Displacements during debrining (left) and principal stresses at the end of debrining (right).

4.2 Mechanical stability during depressurization BC

During depressurization phase BC, the cavern pressure is lowered to atmospheric pressure in 10 days. Figure 10 shows dilation-criterion contours during depressurization BC. At the beginning of depressurization, or the end of debrining, FOS is everywhere larger than 1, meaning there is no dilatant area. At the end of depressurization, large dilatant areas appeared, especially in the overhanging blocks.

4.3 Mechanical stability during repressurization CD

During the repressurization phase CD, the cavern is repressurized back to halmostatic pressure in 10 days. Figure 11 shows effective-stress contours during this repressurization phase. Large areas where effective stress is tensile appear in the overhanging blocks. Figure 12 shows lines oriented in the perpendicular direction of the effective stresses where they are tensile. Possible fractures would develop in these directions.

4.4 Evolution of the state of stress in an overhanging block

To analyze the state of stress in overhanging block #1, a point is considered at a 25.8-m radius and a 703-m depth (the red point in Figure 4).

Figure 13 shows the evolution of FOS related to dilation at this considered location during the whole loading history. Dilation only appears at the end of depressurization phase BC.

Figure 14 shows the evolution of the effective stress at the considered location during the entire loading history. Tensile effective stresses appear briefly shortly during repressurization phase CD.
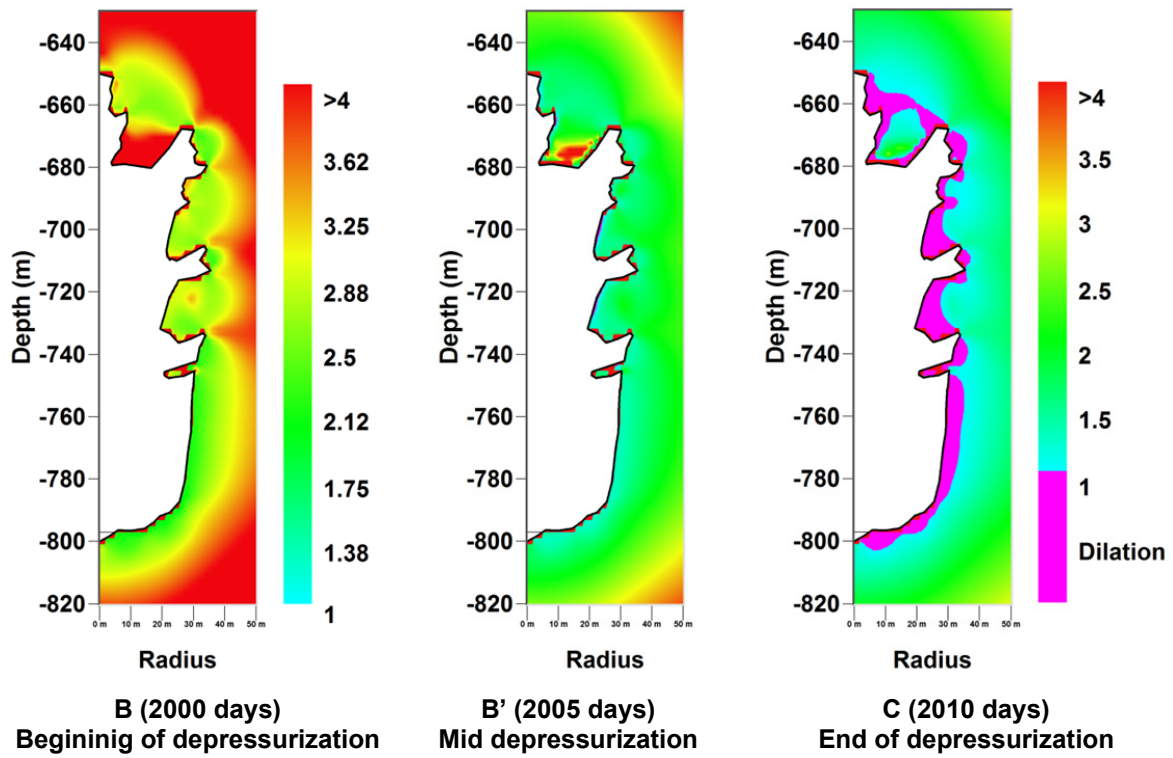
10

B (2000 days)
Begininig of depressurization

B' (2005 days)
Mid depressurization

C (2010 days)
End of depressurization

Figure 10. Dilation-criterion contours (FOS) during depressurization BC.

C (2010 days)
Start of repressurization

C' (2015 days)
Mid repressurization

D (2020 days)
End of repressurization
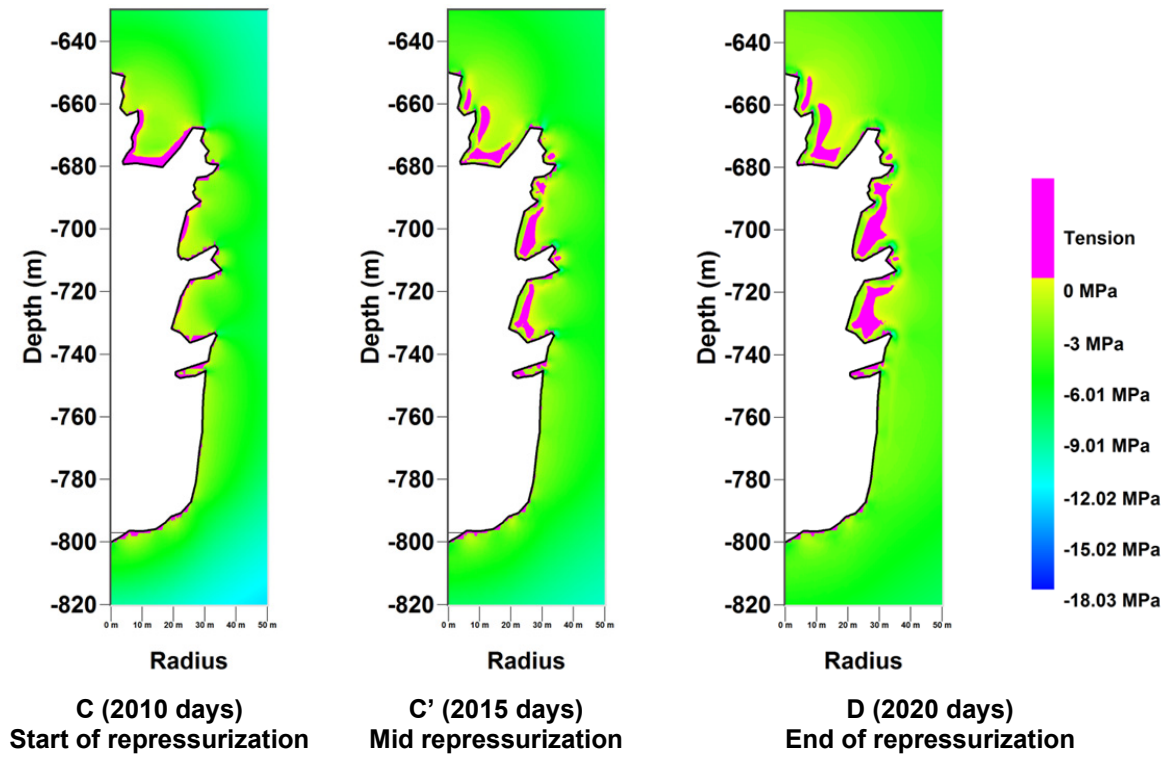
Figure 11. Effective-stress contours during repressurization CD.
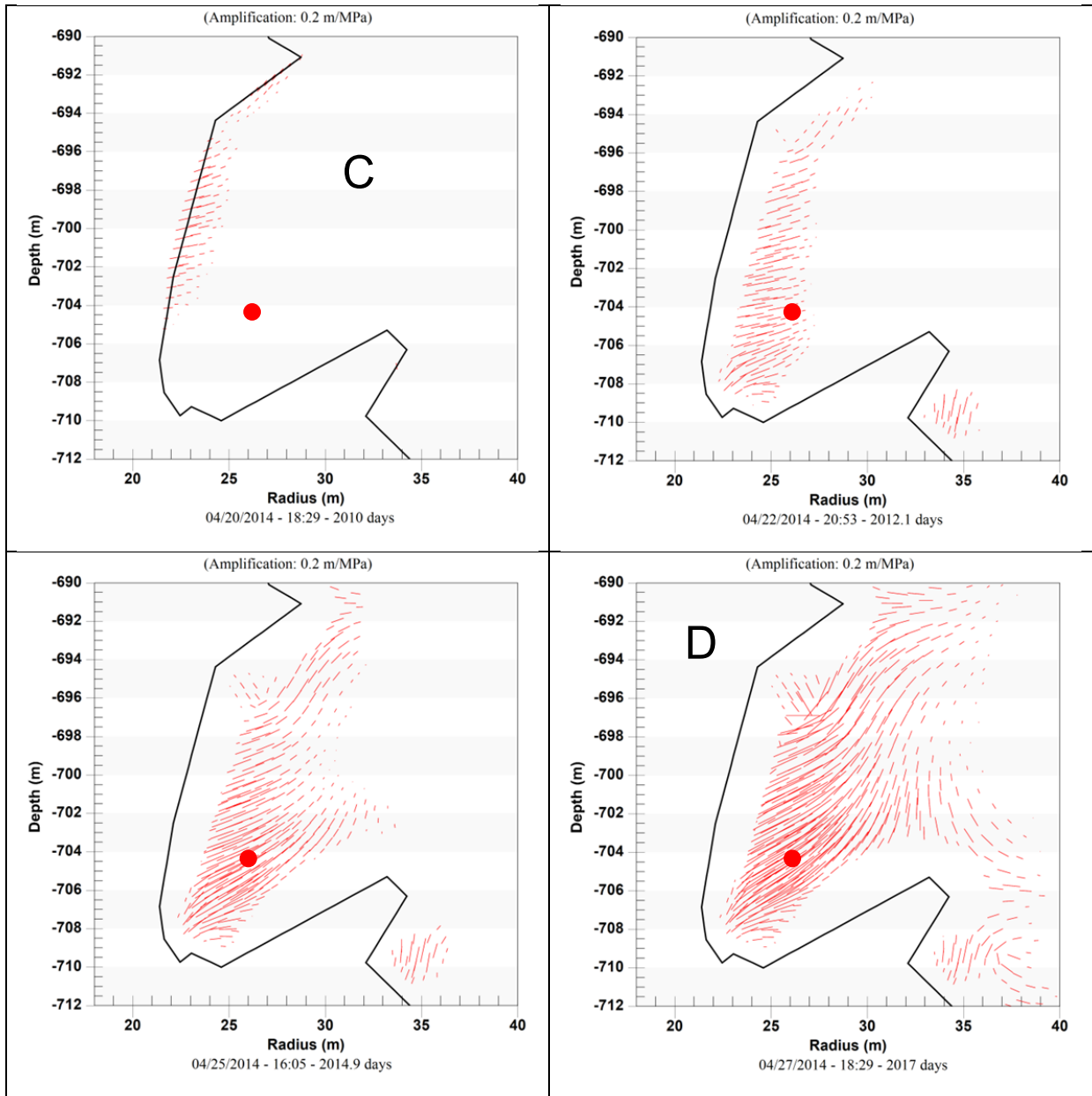
Figure 12. Effective stress in Block #1:
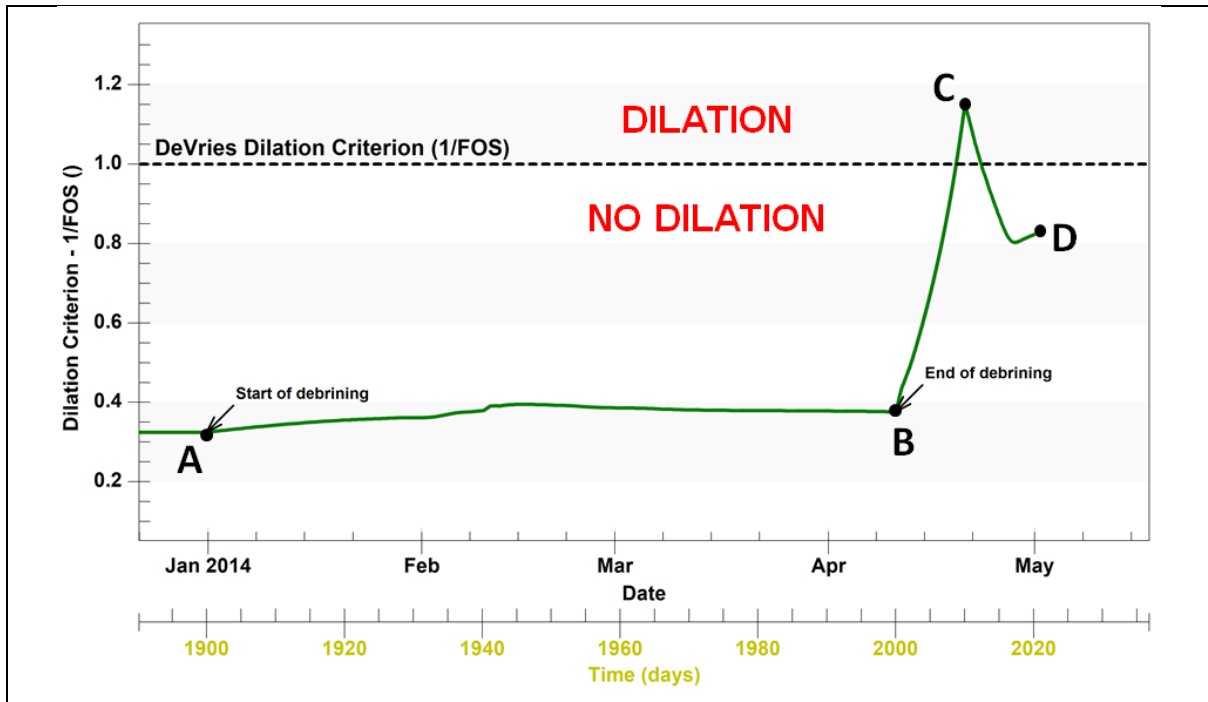**Orientation of possible fractures during repressurization CD.**

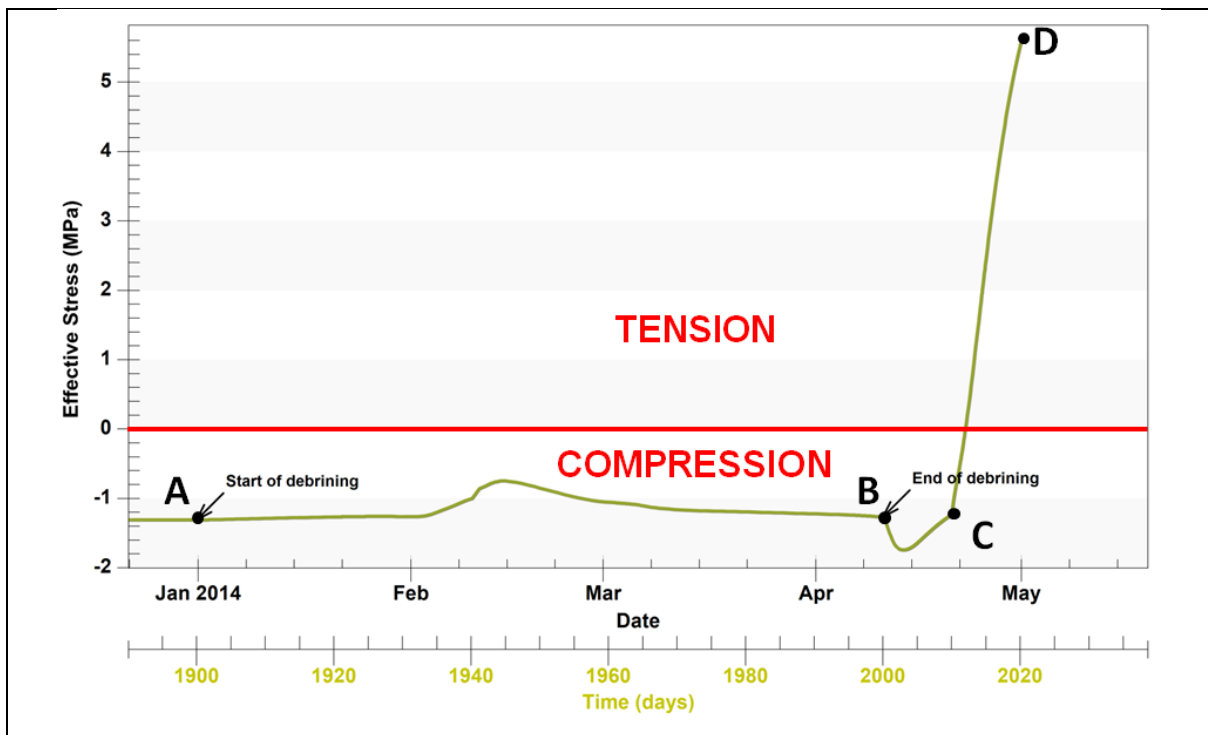**Figure 13. Evolution of the dilation FOS at the considered point in overhanging block #1.**

Figure 14. Evolution of the effective stress at the considered point in block #1.

13

Figure 15 shows the evolution of the state of stress in the invariants plane at the considered point. The path followed by the state of stresses in the invariants plane during the considered loading history is represented together with four dilation criteria: the Spiers (1988), Ratigan (1991) and two DeVries (2006) criteria for compression and extension, respectively.
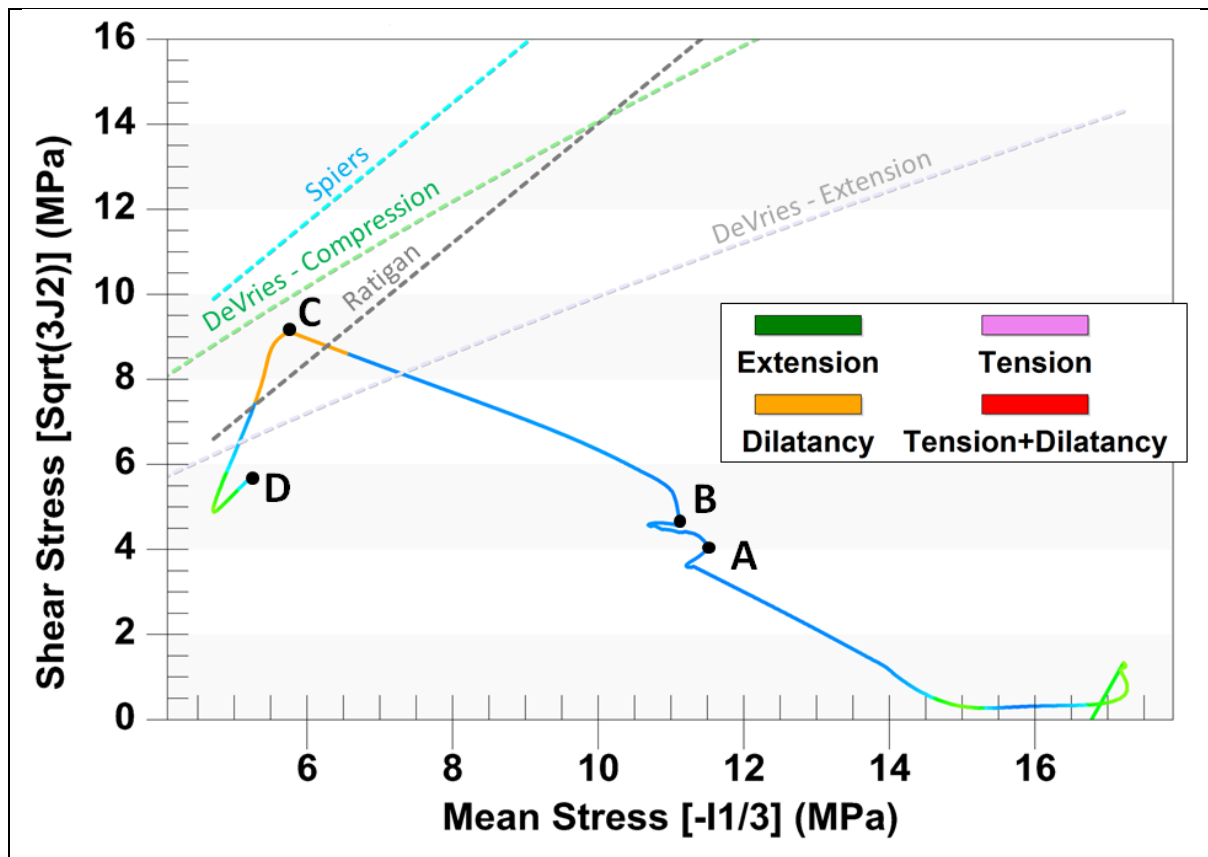

Figure 15. Evolution of the state of stress in the invariants plane at the considered point in overhanging block #1.

4.5 Air lift

An operation called air lift sometimes is performed to lower cavern pressure quickly. It can be performed to remove unstable overhanging blocks. A schematic air-lift process is shown in Figure 16. Compressed air is injected in the tubing while brine is expelled from the annulus. When air reaches the tubing shoe, it bubbles into the annulus and lightens the brine column. A simplified evolution of cavern pressure during an air lift is illustrated in Figure 17. The cavern pressure is lowered by 8 MPa (1160 psi) in only one hour.

Figure 18 shows dilation-criterion contours during air-lift depressurization (BC). Large dilant areas appear in overhanging blocks at the end of depressurization. It is noted that these dilatant areas are smaller that those obtained after a 10-day-long depressurization of the same amplitude after debrining (Figure 10).
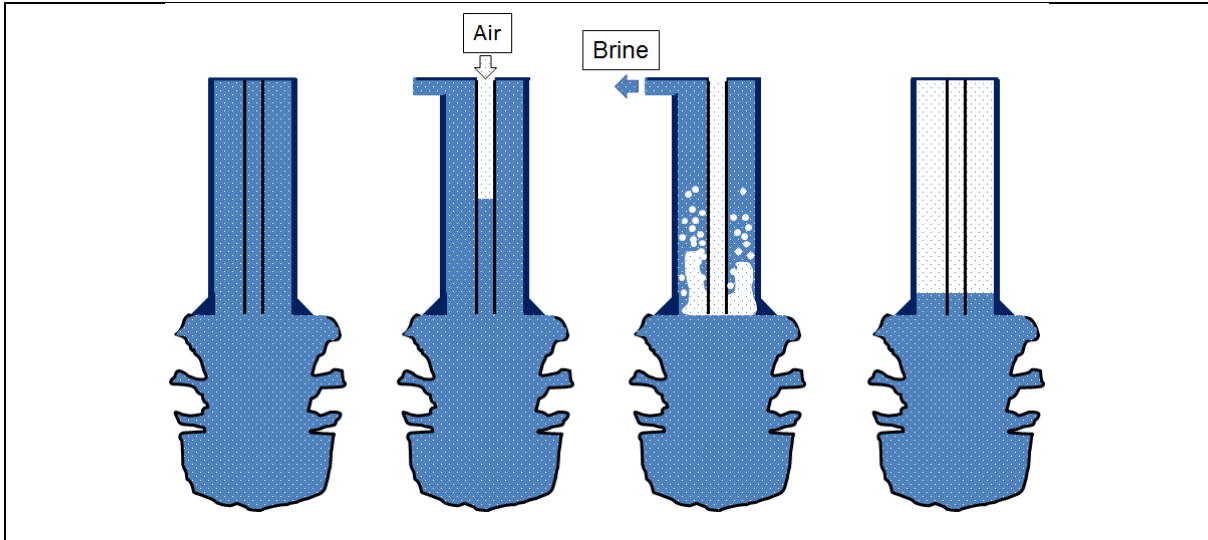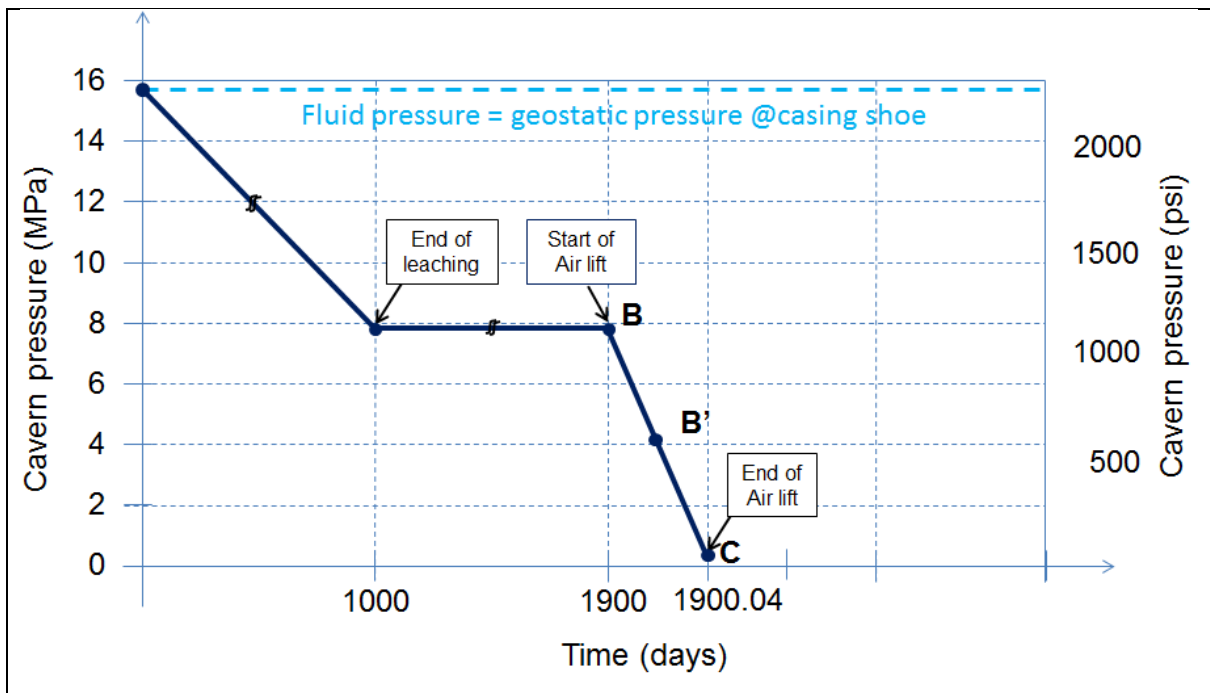
Figure 16.Schematic of an air lift.

Figure 17. Considered evolution of pressure at the cavern top during an air lift.

B (1900 days)
Begininig of depressurization

B'(1900.02 days)
Middle of depressurization

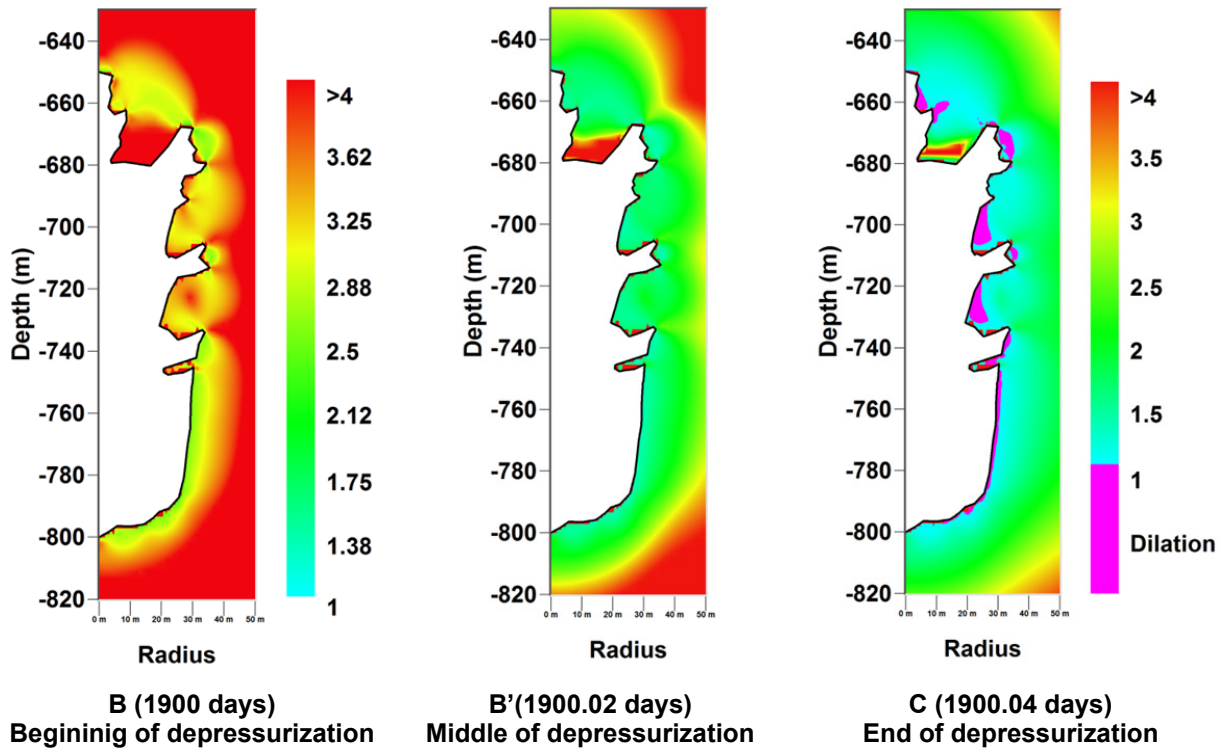**C (1900.04 days)**
End of depressurization

Figure 18. Dilation-criterion contours during air-lift BC.

Figure 19 provides a close-up of dilation-criterion contours in Block #3.

Conclusion

This study shows that the buoyancy effect could explain the fall of overhanging blocks during debrining. When debrining occurs, the tensile effective stress is almost zero in the block, and onset of tensile effective stresses at the upper part of the block can be observed. Because the tensile zone may enlarge when a fracture appears, this process is potentially unstable. If a fracture is open on this side, its spread can be accelerated, as opposed to an existing crack in the lower part of the block. The onset of dilation is also relevant to block falls when debrining is followed by a large pressure decrease. This effect may exist when cavern pressure is lowered to atmospheric pressure during maintenance operations in a CAES facility. During rapid injection, the No-Tensile Effective Stress criterion remains relevant for assessing the thickness of zones that are prone to failure. It also was shown that the onset of dilatancy suggests that block falls can be triggered by an air-lift operation.
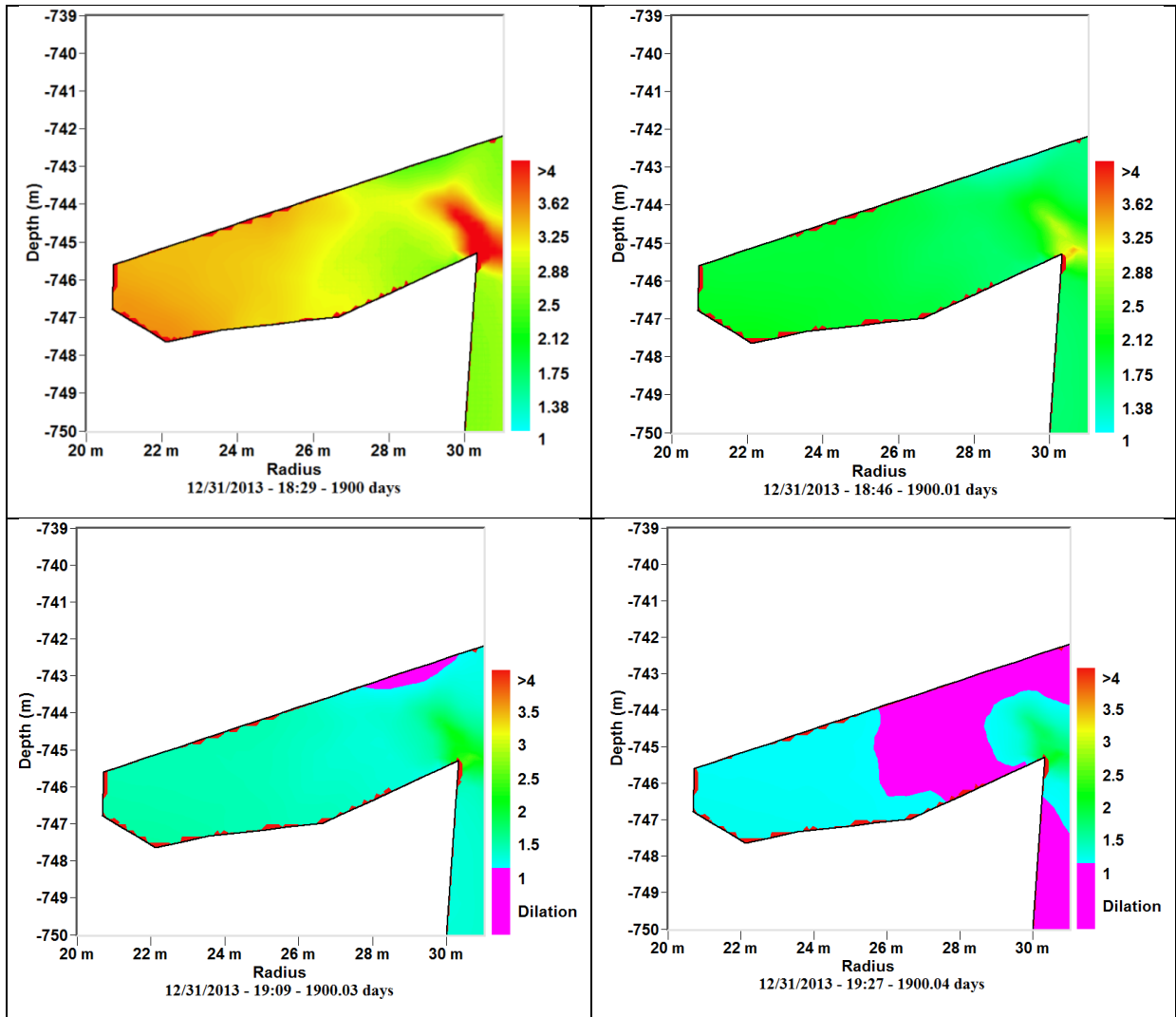
Figure 19. Salt dilation: Factor of safety (FOS) on the lower block during air lift between points B and C.

References

Arnold R.D., DeVries K. L., Nieland J.D. and Tiruneh H. (2011) – Cyclic Fatigue Effects on Mechanical Properties of Salt. *Proc. SMRI Spring Technical Conference*, Galveston, USA, Texas, USA, 51 – 64.

Bauer S., Broome S. and Bronowski D. (2010) – Experimental Deformation of Salt in Cyclic Loading. *Proc. of the Solution Mining Research Institute Spring Technical Conference*, Grand Junction, Colorado, USA, April 25 – 28.

Bauer S., Broome S., Bronowski D., Rinehart A. and Ingraham M.D. (2011) – Experimental Deformation of Salt in Cyclic Loading, Insights from Acoustic Emission Measurements. *Proc. SMRI Spring Technical Conference*, Galveston, USA, Texas, USA, 33 – 49.

Bérest P., Djizanne H., Brouard B. and Hévin G. (2012) – Rapid Depressurizations: Can They Lead to Irreversible Damage? *Proc. SMRI Spring Technical Conference*, Regina, Canada, 63 – 86.

Brouard B., Bérest P. and Karimi-Jafari M. (2007) – Onset of Tensile Effective Stresses in Gas Storage Caverns. *Proc. SMRI Fall Technical conference*, Halifax, Canada 119 – 136.

Brouard B., Frangi A. and Bérest P. (2011) – Mechanical Stability of a Cavern Submitted to High Frequency Cycles. *Proc. SMRI Spring Meeting*, Galveston, Texas, 99 – 116.

Brouard B., Karimi-Jafari M., Bérest P. and Frangi A. (2006) – Using LOCAS Software to Better Understand the Behavior of Salt Caverns. Proc. SMRI Spring Technical Conference, Brussels, Belgium, 273 – 288.

Critescu N.D. and Hunsche U. (1998) – Time Effects in rock mechanics. New York: Wiley, p.342.

Crotogino F., Mohmeyer K.U and Scharf R. (2001) - Huntorf CAES: More than 20 Years of Successful Operation. *Proc. of SMRI Spring Meeting*, Orlando, Florida, 351-362.

DeVries K. L. (2006) – Geomechanical Analyses to Determine the Onset of Dilation around Natural Gas Storage Caverns in Bedded Salt. *Proc. SMRI Spring Meeting*, Brussels, Belgium, 131 – 150.

Devries K. L., Mellegard K. D. and Callahan G. D. (2003) – Cavern Design Using a Salt Damage Criterion: Proof-of-Concept Research Final Report. Proc. of SMRI Technical Conference, Houston, TX, USA.

Djizanne H., Bérest P., Brouard B. (2012) – Tensile Effective Stresses in Hydrocarbon Storage Caverns. Proc. SMRI Fall Technical Conference, Bremen, Germany, 223 – 240.

Dresen R. and Lux K-H., (2011) – Method for Design of Salt Cavern with Respect to High frequency Cycling of Storage Gas. *Proc. the Solution Mining Research Institute Spring Technical Conference*, Galveston, Texas, USA, April 18–19.

Fuenkajorn, K. and Phueakphum, D. (2009) – Effects of Cyclic Loading on the Mechanical Properties of Maha Sarakham Salt, April, 2009 *Suranaree J. Sci. Technol., 16(2):91–102*, Thailand.

Quast P. (1983) - L'installation de Huntorf : plus de trois années de fonctionnement de cavernes à air comprimé. Annales des Mines, 190ème année, n°5-6, mai-juin 1983, 93-102 (in French).

Ratigan J. L., Van Sambeek L. L., DeVries K. L. and Nieland J. D. (1991) – The Influence of Seal Design on the Development of the Disturbed Rock Zone in the WIPP Alcove Seal Tests, RSI-0400, *prepared by RE/SPEC Inc., Rapid City, SD for Sandia National Laboratories, Albuquerque, NM.*

Spiers C. J., Peach C. J., Brzesowsky R.H., Schutjens P.M., Liezenberg J.L. and Zwart H. J. (1988) – Long Term Rheological and Transport Properties of Dry and Wet Salt Rocks. EUR 11848 prepared for Commission of European Communities, by University of Utrecht, Utrecht, The Netherlands.

Staudtmeister K., and Zapf D. (2010): Rock Mechanical Design of Gas Storage Caverns for Seasonal Storage and Cyclic Operations. *Proc. SMRI-Spring Technical Conference*, Grand Junction, Colorado, USA, April 25–28.

Van Sambeek L. L., Ratigan J. L. and Hansen F. D. (1993) – Dilatancy of Rock Salt in Laboratory Test, *Proc. 34th U.S. Symposium on Rock Mechanics*, University of Wisconsin-Madison, Madison, WI, June 24-30. Haimson (ed.), *International Journal of Rock Mechanics and Mining Sciences & Geomechanics Abstracts*, Pergamon Press, Vol 30, N° 7, 735-738.

APPENDIX

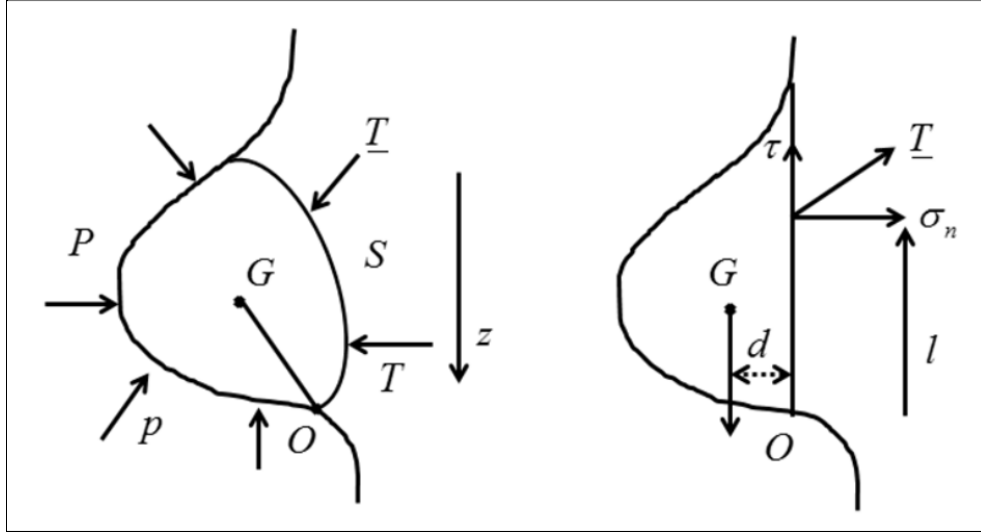**ARCHIMEDES' PRINCIPLE APPLIED TO SALT CAVERNS**

Figure A1 – Schematic diagram.

The pressure, *p*, is applied at the cavern wall. $\underline{T} = -p\underline{n}$

In the solid, and the arbitrary, line S, $\underline{T}$ is the traction vector.

The balance is given by

$$\int_{\Omega} \rho_{sel} g d\Omega + \int_{P} -p\underline{n}dA + \int_{S} \underline{T}dA = 0 \tag{A.1}$$

$$\int_{\Omega} O\underline{M} \wedge \rho_{sel}\underline{g}d\Omega + \int_{p} -O\underline{M} \wedge p\underline{n}dA + \int_{S} O\underline{M} \wedge \underline{T}dA = 0 \tag{A.2}$$

For example, we take the first equation,

$$\int_{\Omega} \rho_{sel}\underline{g}d\Omega + \int_{P+S} -p\underline{n}dA + \int_{S}(T + p\underline{n})dA \tag{A.3}$$

where p along S is equal to p on P at the same depth.

As $gr\underline{a}dP = \rho_F\underline{g}$, where ρ_F represents the buoyancy and ρ_{sel} the weight, then

$$\int_{\Omega}(\rho_{sel} - \rho_F)\underline{g}d\Omega + \int_{S}(\underline{T} + p\underline{n})dA = 0 \tag{A.4}$$

$$\Omega(P_{sel} - P_F)\underline{g} + \int_{S}(\underline{T} + p\underline{n})dA = 0 \tag{A.5}$$

The other equation gives

$$\Omega\left(P_{sel} - P_F\right)O\underline{G} \wedge \underline{g} + \int_S O\underline{M} \wedge \left(\underline{T} + p\underline{n}\right)dA = 0 \tag{A.6}$$

For simplification consider a vertical line.

The shear stress, $\tau \underline{e_z}$, and the effective normal stress, $\sigma_n + p = \underline{n}T + p$, can be identified:

$$\Omega\left(\rho_{sel} - \rho_F\right)g + \int_S \tau dA = 0 \tag{A.7}$$

$$\Omega\left(\rho_{sel} - \rho_F\right)g + \int_S \left(\sigma_n + P\right)dA = 0 \tag{A.8}$$

The effective normal stress, $p + \sigma_n$ (which is not necessarily main) is a void integral, so both tension and compression exist. The vertical shear stress balanced the weight. It increases in average when the size of the outside profile increases.

Furthermore,

$$\Omega\left(\rho_{sel} - \rho_F\right)d = \int l\left(\sigma_n + p\right)dA \tag{A.9}$$

It can be concluded that the horizontal stress is a tension in the upper part and that it increases substantially (or duplicates) when the gas is replaced by the brine because ρ_F becomes almost nil.